Giant multiphoton absorption for THz resonances in silicon hydrogenic donors

Giant multi-photon absorption for THz resonances in silicon hydrogenic donors

MAW van Loon[1], N Stavrias[1], Nguyen H. Le[2], KL Litvinenko[2], PT Greenland[3], CR Pidgeon[4], K Saeedi[1], B Redlich[1], G Aeppli[5,6,7], and BN Murdin[2]

[1]*Radboud University, Institute for Molecules and Materials, FELIX Laboratory, Toernooiveld 7c, 6525 ED Nijmegen, The Netherlands*
[2]*Advanced Technology Institute and SEPNet, University of Surrey, Guildford, GU2 7XH, UK*
[3]*London Centre for Nanotechnology and Department of Physics and Astronomy, University College London, London WC1H 0AH, UK*
[4] *Institute of Photonics and Quantum Science, SUPA, Heriot Watt University, EH14 4AS, UK*
[5]*Laboratory for Solid State Physics, ETH Zurich, Zurich, CH-8093,Switzerland,*
[6]*Institut de Physique, EPF Lausanne, Lausanne, CH-1015, Switzerland,*
[7]*Swiss Light Source, Paul Scherrer Institut, Villigen PSI, CH-5232, Switzerland*

Abstract

The absorption of multiple photons when there is no resonant intermediate state is a non-linear process well known for atomic vapours, dyes and semiconductors. The N-Photon Absorption (NPA) rate for donors in semiconductors scales from hydrogenic atoms in vacuum proportionally with dielectric constant and inversely with effective mass - factors which carry exponents 6N and 4N respectively - implying extremely large enhancements are possible. We observed 1PA, 2PA and 3PA in Si:P with a THz free electron laser and e.g. the 2PA coefficient for 1s-2s at 4.25THz is 400,000,000GM (=10^{-42}cm^{4}s), many orders of magnitude larger than available in other systems. Such high cross-sections allowed us to enter a regime where the NPA cross-section exceeds that of 1PA, i.e. when the intensity approaches the binding energy per Bohr radius squared divided by the uncertainty time (only 3.84MW/cm^2 in silicon), and will enable new kinds of THz quantum control experiments.

Multi-photon transitions[1] are valuable for high frequency resolution metrology[2,3] and high spatial resolution microscopes[4]. Photonic devices relying on such transitions include auto-correlators[5,6], modulators[7,8] and sources of correlated photons[9]. The excitation rate for NPA is proportional to the intensity raised to the power of N for a drive frequency ω_{eg}/N where $\hbar\omega_{eg}$ is the energy separation between the ground (g) and excited (e) states, and N is the number of photons required to achieve a Rydberg transition[1]. The non-linearity in intensity makes the absorption lines sharper, and this effect is therefore attractive for precise measurement of atomic level energies[2,3]. The non-linear coefficients for a hydrogenic oscillator scale with R^{2N}/ω^{2N-3} (see Eqn (2) below) where the effective dipole moment R is a weighted geometric mean of the dipole moments for each step in the N-photon process. In the case of 2PA this scaling is R^4/ω, so a system with small transition energy is attractive, and a system with a large dipole moment is *very* attractive. The silicon donor impurity is a hydrogenic atom with the outer electron orbiting a compact, singly and positively charged ion core. The Coulomb force is greatly reduced by the dielectric screening in the semiconductor environment, as is the effective mass, and the combined effect is to lower the binding energy (Fig 1) and produce enlarged, mesoscale wave functions with an effective Bohr radius of

3.17nm. This results naturally in the desired high R. Here we investigate one-, two-, and three-photon transitions for impurities in silicon which provide giant values of R^{2N}/ω^{2N-3}, comparable or larger even than systems with a near resonant intermediate state[5,6,7,10,11]. Indeed in our experiment the signal to noise of the 2PA is comparable to that for 1PA. Although these experiments made use of the flexible tuning and high power of the free electron laser, ideal for THz non-linear optics experiments, the high coefficients we found open the possibility of high efficiency devices such as photon pair emitters for quantum information[9], or high efficiency spin pumping[12].

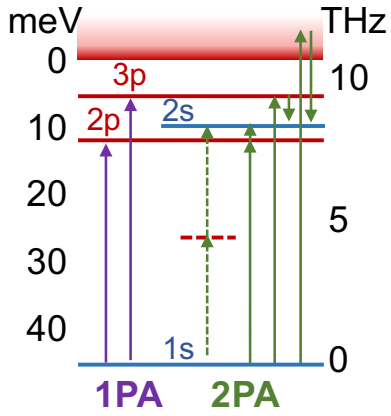

Figure 1. The Si:P level scheme, with some relevant even (blue) and odd parity (red) states (drawn to scale, showing binding energy in meV and transition frequency from the ground state in THz). Purple arrows: 1PA transitions from 1s to the odd parity excited states $2p_0$ and $3p_0$. Green arrows: 2PA transitions from 1s and the even parity excited state 2s is generally thought of as involving a virtual intermediate state (dashed). The actual intermediate states are indicated, and include $2p_0$, $3p_0$ etc and the continuum.

NPA is well known for interband and intervalence band transitions in bulk semiconductors and quantum wells, where different scaling rules apply due to additional factors such as density of states and occupation[5,6,13,14]. Hydrogen-like donors are attractive because of the many orders of magnitude larger quantum coherence lifetimes. 2PA resonances have previously been observed in photo-conductivity for GaAs donors, for which the low binding energy means a magnetic field is required to produce appreciable freeze-out. The 1s-2s transition has been observed at 1T and 0.6THz[15], and the 1s-$3d_{+2}$ at 9T and 4THz[16]. The intensity dependence of the absorption in both works was significantly different from quadratic due to strong phonon couplings, so the authors relied on theoretical prediction of the transition energy for identification of the 2PA, and estimation of the cross-section is not possible. Higher order multi-photon-assisted tunnelling through impurities has also been observed[17]. The only theoretical consideration of NPA for shallow donors is of 2PA for 1s-2s in GaAs and CdTe donors[18,19]. There are no reports of three-photon absorption for hydrogenic impurities. Here we describe a quantitative theoretical and experimental study of the 2PA and 3PA for a common impurity in the most common semiconductor and, in particular, we evaluate the absolute cross-section.

	hydrogen	silicon	units	$\log_{10}$(Si/H)
a_0 (Bohr radius)	0.05292	3.17	nm	1.8
$E_H/2\pi\hbar$ (Hartree energy)	6580	9.63	THz	–2.8
$T = 4/\left(1+\sqrt{\varepsilon_r}\right)^2$	1	0.208		–0.7
$I_a = E_H^2/\hbar a_0^2$ (intensity)	6.436×10^{9}	3.84	MW.cm^{-2}	–9.2
$a_0^4\hbar/E_H$	1.897	$1.67\text{x}10^{10}$	10^{-50}cm^{4}s (=GM)	9.9
$\mu_1 = (2\pi)^2\alpha_{fs}(a_0^2E_H/\hbar)$	0.3335	1.75	cm^2.s^{-1}	0.7
$\mu_2 = \mu_1.8\left(2\pi\alpha_{fs}/I_a\right)$	1.901×10^{-11}	0.167	cm^2.s^{-1}(MW.cm^{-2})$^{-1}$	9.9
$\mu_3 = \mu_1.243\left(2\pi\alpha_{fs}/I_a\right)^2$	4.113×10^{-21}	0.0603	cm^2.s^{-1}(MW.cm^{-2})$^{-2}$	19.2

Table 1. Hydrogen atomic units (4 s.f.) and scaled atomic units for Si donors, and the resulting integrated NPA cross-section coefficients μ_N for N=1-3. The values of the first two quantities for silicon were taken from Ref 24.

For a continuous wave (c.w.) laser beam, the NPA cross-section, σ_N, may be defined by $\hbar\omega_{eg}w_N = \sigma_N TI$ where I is the intensity in the vacuum, and w_N is the c.w. transition rate, i.e. the change in excited state probability per unit time. The coefficient T is a transmission factor appropriate for atoms in a dielectric medium (see Table 1 & Methods for choice of T). As already mentioned, $w_N \propto I^N$, so the absorption cross-section and rate may be written in terms of an intensity- and broadening-independent coefficient, S_N:

$$\sigma_N(\Delta) = \frac{\hbar\omega_{eg}}{TI}w_N = S_N(TI)^{N-1}g_N(\Delta) \tag{1}$$

where $\Delta = \omega_{eg}/N - \omega$ is the detuning and $g_N(\Delta)$ is a lineshape function with $\int g_N d\Delta = 1$. For 1PA, $S_1 = \int \sigma_1 d\Delta$ is just the integrated cross-section, and we refer to S_N in the same way for NPA also. The rate w_N may be found for a homogeneously broadened excited state using N^{th}-order perturbation theory[1] (see Supplementary Methods), within the dipole and rotating wave approximations, whence

$$S_N = \frac{(2\pi)^{N+1}N^{2N-1}\alpha_{fs}^N}{\hbar^{N-1}}\frac{R_N^{2N}}{\omega_{eg}^{2N-3}} \tag{2}$$

where α_{fs} is the fine structure constant, E_H the Hartree energy, a_0 the Bohr radius. In the case of one-photon transitions, the 1PA dipole moment, $R_1 = \left|\boldsymbol{\epsilon}.\mathbf{r}_{eg}\right|$ where $\mathbf{r}_{eg}$ is the matrix element of the position operator between ground and excited states, and $\boldsymbol{\epsilon}$ is a unit vector along the polarization direction. For multi-photon transitions the effective dipole moment, R_N, is a weighted geometric mean of the $\mathbf{r}_{ij}$ involved in the multi-photon transition (Fig 1) with units of length. In the case of 2PA, it is

$$R_2 = \frac{1}{2}\left|\sum_i \frac{\omega_{eg}(\boldsymbol{\epsilon}.\mathbf{r}_{ei})(\boldsymbol{\epsilon}.\mathbf{r}_{ig})}{(\omega_{eg}/2-\omega_{ig})}\right|^{\frac{1}{2}} \tag{3}$$

Although the weights depend on the choice of gauge, the result of the summation is gauge-invariant[20]; here we used the **E**.**r** "multipole" gauge. The equation for a general R_N is given in Methods, and values of R_N for hydrogen[1,21] are shown in Table 2.

The odd parity excited states for Si:P (Fig 1) are well known experimentally from 1PA spectroscopy[22,23,24]. Calculation of the theoretical values of ω_{eg} and $\mathbf{r}_{eg}$ is complicated due to the multi-valley, anisotropic nature of the conduction band of silicon, and the strong effects

of the central cell correction (CCC) potential (a departure from a simple $1/r$ potential analogous to the quantum defect for free atoms) on the ground state[22], but there are well-established predictions for σ_1 that are in good agreement with 1PA experiment[23,25]. The excited states for even N have even parity and also suffer from the CCC[22,26], but they may be accessed experimentally using "two-electron" transitions[27] in the donor-bound exciton luminescence, which includes a (very weak) process where one electron recombines with the hole, and the other electron is excited to a higher state. The photon emitted is down-shifted by an amount equal to the electron excitation energy. Values of ω_{eg} are given in Table 2.

Hydrogen odd N	2p	3p	4p	4f		
$\omega_{eg}/2\pi$ (THz)	2460	2920	3080	3080		
R_1/a_0	0.745	0.298	0.176	0		
R_3/a_0 ††	0.983	0.923	0.885	0.717		
Hydrogen even N	2s	3s	3d	4s	4d	
$\omega_{eg}/2\pi$ (THz)	2500	2900	2900	3100	3100	
R_2/a_0 †	0.858	0.488	0.808	0.358	0.660	
Si:P odd N	$2p_0$	$2p_\pm$	$3p_0$	$4p_0$	$3p_\pm$	$4p_\pm$
$\omega_{eg}/2\pi$ (THz) *	8.22	9.45	9.67	10.19	10.24	10.46
R_1/a_0***	0.209	0.412	0.068	0.039	0.169	0.097
R_3/a_0****	0.303	0.728 (0.32)	0.428	0.388	0.413	0.533
Si:P even N	$2s(A_1)$	$3s(A_1)$	$3d_0(A_1)$	$4s(A_1)$	$3d_2$	$4d_0(A_1)$
$\omega_{eg}/2\pi$ (THz) **	8.51	9.73	10.09	10.24	10.36	10.47
R_2/a_0 ****	0.485 (0.46)	0.435 (0.44)	0.463	0.236	0.436	0.360

Table 2. NPA effective dipole moments and transition energies for multi-photon transitions from the ground state in hydrogen and silicon. All values are theoretical apart from those in brackets, which are experimental from this work. The estimated systematic uncertainty in the experimental R_N^{2N} is an order of magnitude (see Methods), with comparatively negligible random contribution, leading to uncertainty in R_N of a factor of ~2. †Derived from $R_N^N = a_0^N \left|M^{(N)}\right| E_H/\hbar\omega_{eg}$, with $\left|M^{(2)}\right|$ from Ref 1. ††Similarly, with $\left|M^{(3)}\right|$ from Ref 21. *Ref 23. **Ref 26 apart from $3d_2$ Ref 23. ***Derived from oscillator strength in Ref 25 (without CCC, using m^* value given there and ratioed with a_0 from Table 1). ****This work.

It can be seen immediately from Eqns (1) & (2) that the NPA cross-section σ_N and its integral S_N will be large if R_N is large and ω_{eg} is small (for $N \geq 2$); in other words, loosely bound atoms are easier to drive. Since R_N scales with a_0 and $\hbar\omega_{eg}$ scales with E_H, it is convenient to rewrite Eqn (2)

$$S_N = \left(\frac{E_H}{\hbar\omega_{eg}}\right)^{2N-3} \left(\frac{R_N}{a_0}\right)^{2N} \mu_N \tag{4}$$

For a relative dielectric constant ε_r and effective electron mass m_*, $a_0 \propto \varepsilon_r/m_*$ and $E_H \propto m_*/\varepsilon_r^2$, which lead to

$$\mu_N = (2\pi)^2 \alpha_{fs} N^{2N-1} \left(\frac{2\pi\alpha_{fs}}{I_a}\right)^{N-1} \frac{a_0^2 E_H}{\hbar} \propto \frac{\varepsilon_r^{6N-6}}{m_*^{4N-3}} \tag{5}$$

where $I_a = E_H^2/\hbar a_0^2 \propto m_*^4/\varepsilon_r^6$ is the atomic unit of intensity (Table 1). Spherically symmetric hydrogenic atoms with no quantum defect or CCC all have the same $\hbar\omega_{eg}/E_H$ and R_N/a_0, and so variations in the absolute value of S_N are given simply by μ_N. Additional effects like effective mass anisotropy and the CCC are responsible for differences in $\hbar\omega_{eg}/E_H$ and R_N/a_0 and produce changes in the details of the NPA spectrum. Eqn (5) and Table 1 show that μ_N is dramatically larger for Rydberg excitations in Si donors than for H in vacuum: we might expect a ten orders of magnitude increase in the two photon cross-section (Table 1). A heuristic argument suggests that NPA supersedes 1PA when the photon flux approaches one photon per uncertainty time per Bohr radius squared, where the uncertainty time is the energy divided by $\hbar$, which is when I approaches I_a. Eqns (1) & (5) validate this approximation (to within some factors of N, $2\pi\alpha_{fs}$, T etc), and since I_a is nine orders of magnitude smaller for Si:P than for free hydrogen atoms, we expect it to be correspondingly easier to enter an interesting regime.

Results

Calculated multi-photon absorption rates

The remaining unknown in Eqn (4) (and hence in Eqn (1)) is the effective NPA dipole moment. $R_{N\geq 2}$ (given by Eqn (3) for N=2) involves a sum over an infinite number of intermediate states, including the continuum (Fig 1), which must be included as it can carry a significant fraction of the weight[20]. However, the explicit sum can be avoided using the implicit summation technique[1,18] (see Methods). Results for N=2 and 3 for silicon donors calculated within the one band effective mass approximation for polarization along a crystal axis (including longitudinal and transverse valleys but ignoring the effects of the CCC) are shown in Table 2.

Multi-photon absorption spectra

A silicon wafer doped with phosphorus density $1.2\text{x}10^{14}$ cm^{-3} was cooled in a cryostat to 10K. Fig 2 shows the apparatus. We excited the sample with picosecond pulses from the FELIX free electron laser, and measured the spectral density of the photo-conductance signal, F_N, against laser centre frequency, f_L, as shown in Fig 3. The pulses are coherent and bandwidth limited with spectrum shown in Fig 2. Their duration (~10ps) is much shorter than the excited state dephasing time-scales (T_2~160ps[28,29] and the FWHM frequency $\Gamma_{\text{FWHM}}/2\pi$ ~ 50GHz from the small signal absorption line-width of the specific sample) and in this case the excited state probability P_N may also be calculated with N^{th} order perturbation theory (see Supplementary Methods). For pulsed beams, the equivalent of the cross-section (Eqn (1)) is the energy absorbed per pulse per atom, divided by the incident energy per pulse per unit area, D,

$$\frac{\hbar\omega_{eg}P_N}{TD} = S_N(T\tilde{I})^{N-1}G_N(\Delta) \qquad (6)$$

Eqn (6) has the same form as the incoherent c.w. version, Eqn (1), with the c.w. intensity I replaced by an average intensity in the pulse, $\tilde{I}$, defined by $\tilde{I}^{N-1} = \frac{1}{D}\int_{-\infty}^{\infty} I^N dt$, and g_N replaced by G_N, a line shape function of unit area (and of width that scales as the laser spectral width over $\sqrt{N}$). For a Gaussian temporal pulse profile, G_N is also a Gaussian of r.m.s. width $\Delta_L/\sqrt{N}$ and $\tilde{I} = D/\tau_G\sqrt{2\pi N^{1/(N-1)}}$ where Δ_L is the r.m.s. width of the laser intensity spectrum, Fig 2, and $\tau_G = 1/2\Delta_L$ is the r.m.s. duration of the temporal intensity profile.

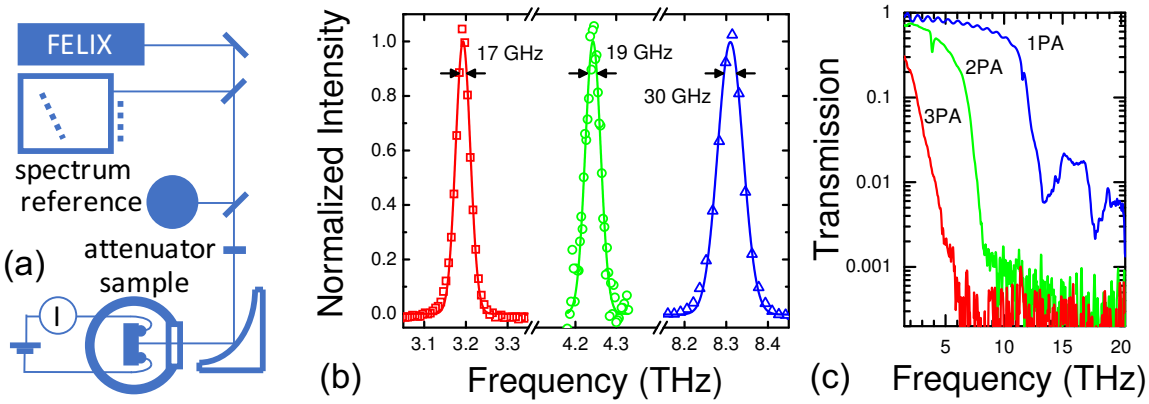

Figure 2. The experiment. a) Schematic of the experimental setup showing the photo-conductance circuit sample, in a cryostat, and the simultaneous reference detector and grating spectrum analyser. b) Example experimental FELIX spectra (symbols) with different line-centres. The corresponding r.m.s. spectral width in GHz ($\Delta_L/2\pi$) is given for each, and a Gaussian fit is shown as a solid line. c). Spectra of filters used for each NPA experiment.

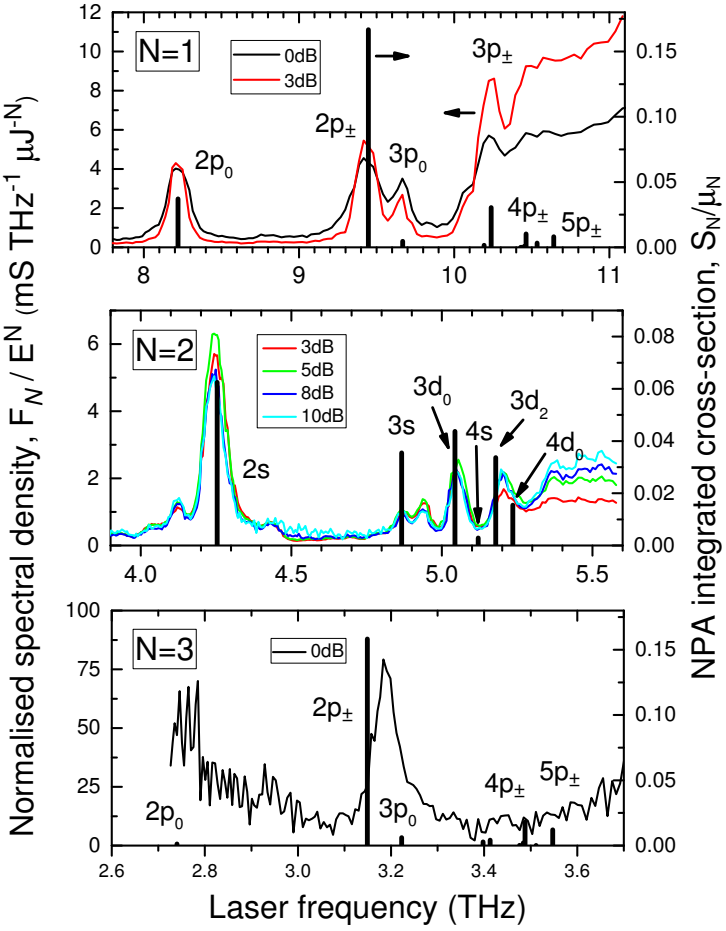

Figure 3. N-photon photo-conductance spectra for various laser attenuations. The abscissae are the laser frequency $f_L=\omega_L/2\pi$ and each panel has Nf_L aligned with the others. The spectral density of the photo-conductance signal, F_N, has been normalised by E^N where $E(f_L)$ is the measured picopulse energy (left ordinate). The expected position, $\omega_{eg}/2\pi N$, and integrated cross-section, S_N/μ_N (right ordinate), of some NPA transitions are indicated with vertical bars using $\omega_{eg}/2\pi$ and theoretical R_N values for Si:P from Table 2.

Eqn (6) suggests that the excitation is proportional to E^N, where E is the laser picopulse energy (proportional to D and I). We controlled E using an attenuator comprising wire-mesh filters, and monitored it continuously with a reference pyroelectric detector. In both 1PA and 2PA cases F_N/E^N is clearly independent of attenuation as shown in Fig 3, indicating that the 1PA is linear with intensity and the 2PA is quadratic, as expected. It is notable that because of the giant coefficients the signal to noise is comparable for both 1PA and 2PA spectra, for the same sample and the same FELIX macropulse energy. There is some evidence of saturation in the continuum response at the high frequency end of the 1PA and 2PA spectra. The 3PA resonance was only observed at the highest available FELIX power (given the current focusing arrangement).

Experimental multi-photon cross-sections

We fitted Gaussians to the well resolved peaks in F_N, and their areas, $Y_N = \int F_N \, df_L$, are shown Fig 4. A power-law fit $Y_N \propto E^N$ was very close to expectation, though the data indicate an exponent slightly higher than N. This might be because the laser produces a small intensity-dependent heating of the sample that raises the thermal-ionization at higher power, or it might be because the thermal-ionization is assisted by field-ionization at high power. Indeed the combination of phonons and high THz fields is known to produce an intensity dependent tunneling ionization in impurities at high power when pumping off-resonance[30,31] and it seems likely that this could be responsible for the deviation from the perturbation result of a simple power law in this case. The averaging over the laser spot means that the lower intensity parts with larger area dominate, making the non-perturbative corrections small. To examine the non-perturbative corrections in detail would require uniform excitation.

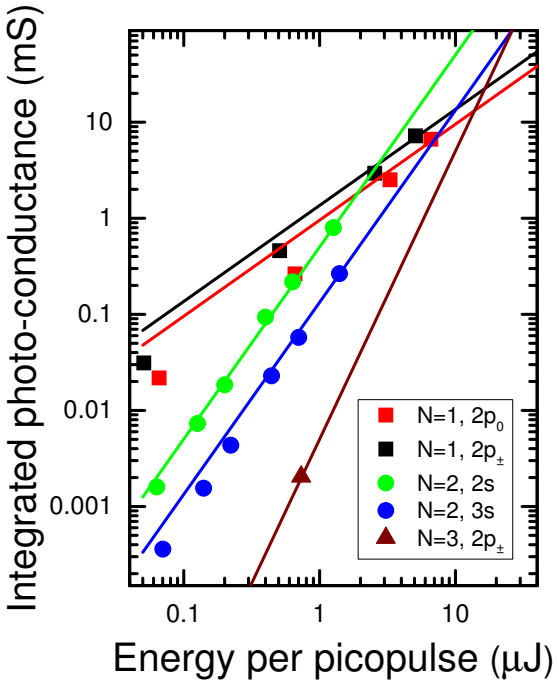

Fig 4. The photo-conductance signal strength for some transitions from Fig 3. The ordinate is the area under the un-normalized lines from Fig 3, $Y_N = \int F_N \, df_L$. The abscissa is the picopulse energy. The right-most data-point on each line corresponds with the 0dB condition from Fig 3, and the difference in the 0dB point from line to line is due to the variation in FELIX output as a function of frequency. Lines are power law fits with fixed integer exponents.

We can extract absolute values of effective multi-photon dipole moment $R_N(1s\rightarrow e)$ from Fig 4 by comparing the NPA transition with a nearby 1PA transition of known R_1. We assume that for energetically nearby excited states $Y_N \propto P_N$ with the same proportionality constant (see Methods for more discussion of this assumption, and other potential sources and scale of systematic error). For example, using the theoretical $R_1(1s\rightarrow 2p_0)$ and $R_2(1s\rightarrow 2s)$ values from Table 2 in Eqn (6), we expect the 2PA 1s→2s absorption to exceed that of 1PA $1s\rightarrow 2p_0$ with an incident pulse energy of 1.5μJ, corresponding to energy density of 0.56mJ/cm^2, an intensity of 42MW/cm^2, and an electric field amplitude of 180kV/cm (all values in vacuum outside the sample). Likewise the 2PA 1s→3s absorption should exceed that of 1PA $1s\rightarrow 2p_\pm$ with a pulse energy of 10μJ (330 MW/cm^2, 230kV/cm), and the 3PA $1s\rightarrow 2p_\pm$ absorption should exceed that of 1PA $1s\rightarrow 2p_\pm$ with a pulse energy of 1.4μJ (35MW/cm^2, 75kV/cm). The experimental results for 2PA of Fig 4 are all within an order of magnitude of these predictions, and the resulting experimental multi-photon dipole moments, R_N, are all within about a factor of two of the theory predictions in Table 2.

Discussion

Our observation is that the picopulse energies and intensities produced by the free electron laser are of the correct scale for substantial multiphoton absorption in Si:P. It is the small E_H and large a_0 for Si:P, and the high power of the free electron laser which allow entry into this interesting highly non-linear regime.

Going into more detail, the relative strengths of the transitions on Fig 3 agree with the NPA coefficients from the calculated effective dipole moments of Table 2. Since R_N is large (and of order a_0 as expected), it is clear that S_N and hence σ_N are also large. Taking the theoretical 2PA dipole moment for the 1s→2s transition (which is in good agreement with experiment, as shown above), $R_2(1s\rightarrow 2s)$ = 1.54nm (Tables 1&2) and produces an integrated cross-section of $S_2(1s\rightarrow 2s) = 1.05\times10^{-2}$ cm^{2}s^{-1}(MW/cm^2)$^{-1}$ using Eqn (4). Assuming the excited state is Gaussian inhomogeneously broadened with the same linewidth as the 1PA lines (in which case $g_N(0) = 2N\sqrt{\ln 2/\pi}\Gamma_{\mathrm{FWHM}}^{-1}$, where $\Gamma_{\mathrm{FWHM}}/2\pi$ = 50GHz mentioned above) our Si:P donor produces a peak cross-section of $S_2 g_2(0)=6.2\times10^{-14}$ cm^2(MW/cm^2)$^{-1}$. The peak 2PA absorption rate per oscillator divided by the square of the photon fluence, $\delta = \left(\hbar\omega_{eg}/2I\right)^2 w_2 = T^2\hbar\omega_{eg}S_2 g_2(0)/4$, is often quoted in units of Goeppert-Mayer, 1GM = 10^{-50} cm^{4}s. For our Si:P donor δ_{1s-2s} = 400,000,000 GM. The NPA coefficient for bulk materials or macroscopic ensembles of oscillators, called K_N (or sometimes β and γ for 2PA and 3PA respectively), is defined by $dI/dz = -K_N I^N = -\sigma_N n_{3D} I$, i.e.$K_N = n_{3D} S_N g_N(0)$. We obtain $K_2(1s\rightarrow 2s)$ = 7.5 cm^{-1}(MW/cm^2)$^{-1}$. In the case of 3PA we have $S_3(1s\rightarrow 2p_\pm) = 9.5\times10^{-3}$ cm^{2}s^{-1}(MW/cm^2)$^{-2}$ and hence $K_3(1s\rightarrow 2p_\pm)$ = 10 cm^{-1}(MW/cm^2)$^{-2}$.

The values of (integrated) cross-section are very large compared with those for other atoms and molecules. The Si:P integrated 2PA cross-section S_2 is about 10 orders of magnitude larger than for hydrogen. Recall that $S_2 \propto R_2^4/\omega$: some of the improvement is due to the fact that ω is a few orders of magnitude smaller, but most of it is due to the large R_2 (for hydrogen, $R_2(1s\rightarrow 2s)$ = 0.0454nm, Tables 1&2). The Si:P integrated cross-section for 1s→2s is 3 orders of magnitude larger than for the atomic rubidium 2PA transition $5S_{1/2} \rightarrow 5D_{5/2}$ which has a near resonant intermediate $5P_{3/2}$ state ($S_2 = 5\times10^{-6}$ cm^{2}s^{-1}(MW/cm^2)$^{-1}$, $\omega_{SD}/2\pi$ = 760THz)[32]. The values of molecular coefficient are also many orders of magnitude larger than for common molecular dyes in the visible (~500THz) which range from δ~0.1-100 GM[33], though there are reports of up to 1,000GM[4]. In quantum dots, biexciton creation

by 2PA is very nearly resonant with the single exciton intermediate state and although 2PA as strong as 1PA has been observed[10] it was not possible to extract the absolute dipole moment.

The macroscopic coefficients for our sample of dilute 0D oscillators are comparable with bulk and 2D semiconductors, and could easily be increased. In bulk semiconductors the interband K_2 increases as the bandgap decreases, and the largest reported values are for bulk InSb, for which[13] K_2~2 $cm^{-1}(MW/cm^2)^{-1}$at 30THz. For comparison in silicon in the near IR at around[34] 300THz K_2~0.001-0.002 $cm^{-1}(MW/cm^2)^{-1}$, and in germanium it is similar at the indirect gap[35]. For intervalence band transitions in p-Ge at 3THz $K_N I^N$ ~ 120cm^{-1} at 1MW/cm^2 for N=2-4 meaning[14] K_2~120 $cm^{-1}(MW/cm^2)^{-1}$. In 2D semiconductors there is a possibility for engineering the quantum well (QW) profile so as to achieve resonance of the intermediate state. Simple GaAs QWs have produced[36] K_2~5 $cm^{-1}(MW/cm^2)^{-1}$at 30THz while resonantly engineered GaAs QWs have given[5] K_2~13,000 $cm^{-1}(MW/cm^2)^{-1}$at 30THz. In the case of 3PA quantitative data is sparse: the coefficient for silicon in the mid-IR[37] is K_3~1 to 2x10^{-9} $cm^{-1}(MW/cm^2)^{-2}$. It is not unreasonable to imagine that for our silicon donor samples we could increase n_{3D} by 2 orders of magnitude, or we could increase $g_2(0)$ by more than an order of magnitude using a cleaner sample, so we could improve our value relatively easily, without the requirement for engineering intermediate state resonances. Additionally we could increase the sample thickness to increase the interaction length.

The very large 2PA and 3PA cross-sections for which the very simple expression of Eqn (5) sets the scale are among the highest ever recorded for a discrete oscillator system, and even at the dilute concentration of the sample we used they are about as high as the highest of any bulk semiconductor. With some simple changes to the sample they could rival the highest available even in engineered quantum well structures with resonant intermediate states. The fact that the transitions are at low frequency is only partly responsible, and it is the very large dipole moment, due to the mesoscopic extent of the donor wavefunctions, that dominates. The experiments open the interesting possibility of using pulses with half and perhaps even one third that of Rydberg transition energies for quantum control of the excited state orbitals[10]. This has several potential advantages. The first is that of accessing new excited states with different symmetry, e.g. the isotropic 2s rather than the axial 2p states used previously[28,38,39,40,41]. The second is that of moving from the Rydberg energies of order 10THz, difficult to reach for non-FEL sources, towards the region near a few THz, which is where certain QCL's[42] as well as mixing crystals[43] produce significant radiation. Current power levels ranging up to 1kW only allow production of order 1MW/cm^2 in free space, but near-field enhancements used for alkali atoms in the visible[7,11,32] are relatively straight-forward for the long wavelengths of THz photons and should make this enough to enter into the quantum control regime hitherto examined for single photon resonances.

References

1 Gontier, Y. & Trahin, M. On The multiphoton absorption in atomic Hydrogen. Phys. Lett. A 36, 463-464 (1971).
2 Foot, C. J., Couillaud, B., Beausoleil, R. G. & Hänsch, T. W. Continuous-wave two-photon spectroscopy of the 1S-2S transition in hydrogen. Phys. Rev. Lett. 54, 1913-1916 (1985).
3 Žitnik, M. et al. High resolution multiphoton spectroscopy by a tunable free-electron-laser light. Phys. Rev. Lett. 113, 193201 (2014).
4 Albota, M., et al. Design of organic molecules with large two-photon absorption cross sections. Science 281, 1653-1656 (1998).

5 Schneider, H., Maier, T., Liu, H.C., Walther, M. & Koidl, P. Ultrasensitive femtosecond two-photon detector with resonantly enhanced nonlinear absorption. Opt. Lett. 30, 287-289 (2005).
6 Schneider, H. et al. Terahertz two-photon quantum well infrared photodetector. Opt. Lett. 17, 12279-12284 (2009)
7 Venkataraman, V., Saha, K., Londero, P. & Gaeta, A. L. Few-photon all-optical modulation in a photonic band-gap fiber. Phys. Rev. Lett. 107, 193902 (2011).
8 Atanasov, R., Haché, A., Hughes, J. L. P., van Driel, H. M. & Sipe, J.E. Coherent control of photocurrent generation in bulk semiconductors. Phys. Rev. Lett. 76, 1703-1706 (1996).
9 Hayat, A., Ginzburg, P. & Orenstein, M. Observation of two-photon emission from semiconductors. Nat. Photon. 2, 238-241 (2008).
10 Stufler, S. et al. Two-photon Rabi oscillations in a single $In_xGa_{1-x}As/GaAs$ quantum dot, Phys. Rev. B 73, 125304 (2006).
11 Hendrickson, S.M., Lai, M.M., Pittman, T.B. & Franson, J.D. Observation of two-photon absorption at low power levels using tapered optical fibers in rubidium vapor. Phys. Rev. Lett. 105, 173602 (2010).
12 Gullans, M.J. & Taylor, J.M. Optical control of donor spin qubits in silicon. Phys. Rev. B 92, 195411 (2015).
13 Murdin, B.N. et al. Infrared free-electron laser measurement of power limiting by two-photon absorption in InSb. Opt. Quantum Electron. 25.171-175 (1993).
14 Ganichev, S.D. et al. Multiphoton absorption in semiconductors at submillimeter wavelengths. Sov. Phys. JETP 64, 729-737 (1986).
15 Böhm, W., Ettlinger E. & Prettl, W. Far-infrared two-photon transitions in n-GaAs. Phys. Rev. Lett. 47, 1198-1201 (1981).
16 Planken, P.C.M. et al. Using far-infrared two-photon excitation to measure the resonant-polaron effect in the Reststrahlen band of GaAs:Si. Opt. Commun. 124, 258-262, (1996).
17 Zeuner, S., Allen, S.J., Maranowski, K.D. & Gossard, A.C. Photon-assisted tunneling in GaAs/AlGaAs superlattices up to room temperature. Appl. Phys. Lett. 69, 2689-2691 (1996).
18 Golka, J. & Mostowski, J. Two-photon spectroscopy of shallow donor states in semiconductors. Phys. Rev. B 18, 2755-2760 (1978).
19 Bassani, F. & Quattropani, A. Two-photon spectroscopy of shallow centers in semiconductors. Solid State Commun. 53, 1077-1081, (1985).
20 Bassani, F., Forney, J.-J. & Quattropani, A. Choice of gauge in two-photon transitions: 1s−2s transition in atomic hydrogen. Phys. Rev. Lett. 39, 1070-1073 (1977).
21 Thayyullathil, R. B., Radhakrishnan, R. & Seema, M. Three-photon transitions from ground state to bound states in atomic hydrogen. J. Phys. A: Math. Gen. 36 8473–8478 (2003).
22 Kohn, W. & Luttinger, J.M. Theory of donor states in silicon. Phys. Rev. 98 915-922 (1955).
23 Pajot, B. Donor and donor-like EM spectra. in Optical absorption of impurities and defects in semiconducting crystals: hydrogen-like centres. (Springer, 2009).
24 Murdin, B.N. et al. Si:P as a laboratory analogue for hydrogen on high magnetic field white dwarf stars. Nat. Commun. 4, 1469 (2013).
25 Clauws, P., Broeckx, J., Rotsaert, E. & Vennik, J. Oscillator strengths of shallow impurity spectra in germanium and silicon. Phys. Rev. B 38, 12377-12382 (1988).

26 Chang, Y.C., McGill, T. C. & Smith, D.L. Model Hamiltonian of donors in indirect-gap materials. Phys. Rev. B 23 4169-4182 (1981).
27 Sauer, R. Optical determination of highly excited s-like donor states in silicon. J. Lumines. 12, 495-499 (1976).
28 Greenland, P.T. et al. Coherent control of Rydberg states in silicon. Nature 465, 1057-1061 (2010).
29 Karaiskaj, D., Stotz, J.A.H., Meyer, T., Thewalt, M.L.W. & Cardona, M. Impurity absorption spectroscopy in ^{28}Si: the importance of inhomogeneous isotope broadening. Phys. Rev. Lett., 90, 186402 (2003).
30 Ganichev, S.D., Prettl, W. & Huggard, P. G. Phonon assisted tunnel ionization of deep impurities in the electric field of far-infrared radiation. Phys. Rev. Lett. 71, 3882-3885 (1993).
31 Ganichev, S. D. et al. Carrier tunneling in high-frequency electric fields. Phys. Rev. Lett. 80, 2409-2412 (1998).
32 Saha, K., Venkataraman, V., Londero, P. & Gaeta, A. L. Enhanced two-photon absorption in a hollow-core photonic-band-gap fiber. Phys Rev A 83, 033833 (2011).
33 So, P.T.C., Dong, C.Y., Masters, B.R. & Berland, K.M. Two-photon excitation fluorescence microscopy. Annu. Rev. Biomed. Eng. 2, 399–429 (2000).
34 Bristow, A.D., Rotenberg, N. & van Driel, H.M. Two-photon absorption and Kerr coefficients of silicon for 850–2200 nm. Appl. Phys. Lett. 90, 191104 (2007).
35 Tuncel, E. et al. Free-electron laser studies of direct and indirect two-photon absorption in germanium. Phys. Rev. Lett. 70, 4146-4149 (1993).
36 Zavriyev, A., Dupont, E., Corkum, P. B., Liu, H. C. & Biglov, Z. Direct autocorrelation measurements of mid-infrared picosecond pulses by quantum-well devices. Opt. Lett. 20, 1886-1888 (1995).
37 Wang, T. et al. Multi-photon absorption and third-order nonlinearity in silicon at mid-infrared wavelengths. Opt. Express 21, 32192-32198 (2013).
38 Chick, S. et al. Coherent superpositions of three states for phosphorous donors in silicon prepared using THz radiation. Nat. Commun. 8, 16038 (2017)
39 Litvinenko, K. L. et al. Weak probe readout of coherent impurity orbital superpositions in silicon. Phys. Rev. B 94, 235207 (2016)
40 Greenland, P. T. et al. Quantitative analysis of electrically detected Ramsey fringes in P-doped Si. Phys. Rev. B 92, 165310 (2015)
41 Litvinenko, K. L. et al. Coherent creation and destruction of orbital wavepackets in Si:P with electrical and terahertz read-out. Nat. Commun. 6, 6549 (2015)
42 Li, L.H. et al. et al. Multi-Watt high-power THz frequency quantum cascade lasers. Electron. Lett. 53, 799-800 (2017).
43 Tochitsky, S.Y., Sung, C., Trubnick, S.E., Joshi, C. & Vodopyanov, K.L. High-power tunable, 0.5-3 THz radiation source based on nonlinear difference frequency mixing of CO_2 laser lines. J. Opt. Soc. Am. B 24, 2509-2516 (2007).
44 Knippels, G. M. H. et al. Generation and complete electric-field characterization of intense ultrashort tunable far-infrared laser pulses. Phys. Rev. Lett. 83, 1578 (1999)
45 Vinh, N. Q. et al. Silicon as a model ion trap: Time domain measurements of donor Rydberg states. Proc. Natl. Acad. Sci. USA 105, 10649-10653 (2008)

Acknowledgments

We gratefully acknowledge the Nederlandse Organisatie voor Wetenschappelijk Onderzoek (NWO) for the support of the FELIX Laboratory and the financial support from the UK

Engineering and Physical Sciences Research Council [COMPASSS/ADDRFSS, Grant No. EP/M009564/1]. B.N.M. is grateful for a Royal Society Wolfson Research Merit Award. We are also thank Dr S. Pavlov and Profs M. Thewalt, G. Davies and E. Linfield for useful discussions.

Author Contributions

BNM designed the project, MAWL, NS, KS, BR, PTG performed the experiments, NHL and BNM provided theoretical methods and calculations, BNM, KLL, CRP, and GA wrote the paper.

Additional information

Correspondence and requests for materials should be addressed to BNM.

Competing interests

The authors declare no competing financial interests.

Methods

Calculating the multi-photon matrix elements

The general N-photon matrix element in the **E.r** gauge is given by (see Supplementary Methods)

$$R_{N\geq 2} = \frac{1}{N}\left|\sum_d \dots \sum_b \sum_a \frac{\omega_{eg}^{N-1}(\boldsymbol{\epsilon}.\mathbf{r}_{ed}) \dots (\boldsymbol{\epsilon}.\mathbf{r}_{ba})(\boldsymbol{\epsilon}.\mathbf{r}_{ag})}{\left((N-1)\omega_{eg}/N - \omega_{dg}\right) \dots \left(2\omega_{eg}/N - \omega_{bg}\right)\left(\omega_{eg}/N - \omega_{ag}\right)}\right|^{\frac{1}{N}}$$

It involves a sum over an infinite number of intermediate states (Fig 1), including the continuum which must be included as it can carry a significant fraction of the weight. The sum can be avoided using the implicit summation technique developed by (among others) Gontier and Trahin[1]. We rewrite $R_{N\geq 2}$ as an iterative set

$$R_{N\geq 2} = \frac{1}{N}|\langle e|r|D\rangle|^{1/N}$$

where $r = \boldsymbol{\epsilon}.\mathbf{r}$ and

$$|D\rangle = \omega_{eg}\sum_d \frac{|d\rangle\langle d|}{\left((N-1)\omega_{eg} - N\omega_{dg}\right)} r|C\rangle$$

$$\vdots$$

$$|B\rangle = \omega_{eg}\sum_b \frac{|b\rangle\langle b|}{\left(2\omega_{eg} - N\omega_{bg}\right)} r|A\rangle$$

$$|A\rangle = \omega_{eg}\sum_a \frac{|a\rangle\langle a|}{\left(\omega_{eg} - N\omega_{ag}\right)} r|g\rangle$$

where $|a\rangle, |b\rangle \dots |d\rangle$ and $|e\rangle$ and $|g\rangle$ are all solutions of $\hat{H}|k\rangle = \hbar\omega_k|k\rangle$, and $\hat{H}$ is the Hamiltonian for the atom in the dark[22]. Hence, making use of the fact that $\sum_k |k\rangle\langle k| = \hat{I}$ is the identity, the functions $|A\rangle, |B\rangle \dots |D\rangle$ are solutions of the set of 2nd order partial differential equations (PDEs)

$$\left(\hbar\omega_e + (N-1)\hbar\omega_g - N\hat{H}\right)|A\rangle = \hbar\omega_{eg} r|g\rangle$$

$$\left(2\hbar\omega_e + (N-2)\hbar\omega_g - N\hat{H}\right)|B\rangle = \hbar\omega_{eg} r|A\rangle$$

$$\vdots$$

$$\left((N-1)\hbar\omega_e + \hbar\omega_g - N\widehat{H}\right)|D\rangle = \hbar\omega_{eg} r|C\rangle$$

These PDEs were integrated by sequential application of the finite element method, and finally used to integrate R_N^{2N}. We took $\widehat{H}$ from the one band effective mass approximation, combining the longitudinal and transverse valley wavefunctions according to the A_1, E, and T_2 states of T_d symmetry[22,23] but ignoring the energy effects of the CCC. Following the experimental configuration, the polarization $\boldsymbol{\epsilon}$ was along a crystal axis.

Experimental procedure

The non-linearity of NPA for $N>1$ means that unless the atomic density is very high, the number of photons absorbed is very low, and a simple transmission measurement is not possible. Often in atomic vapour the detection is via luminescence from a transition to an intermediate state, and in this work we make use of the thermal ionization out of the excited state to produce a photo-current in the semiconductor host, in what is known as Photo-Thermal Ionization Spectroscopy (PTIS). At the temperature of the experiment, donors in thermal equilibrium with the lattice are all in their ground state (for which E_b/k_B ~500K where E_b is the binding energy), and the current is negligible, but when atoms are in excited states (for which E_b/k_B <~100K) the thermal excitations of the lattice ionize enough impurities to produce an observable photocurrent.

The sample was placed in a vacuum on the cold-finger of a continuous flow helium cooled cryostat with a polypropylene film window (Fig 2). The temperature of the sample was monitored with a rhodium iron sensor mounted on the cold-head just above the sample. The laser irradiation at the average power used has negligible effect on the sample temperature, but black-body radiation from the windows raises it somewhat: we estimate that it was about 10K for these experiments.

The sample used was a 0.5cm square, cut from a commercial Czochralski silicon wafer, 0.05cm thick with plane parallel polish on both (100) faces. It was bulk doped with phosphorus with concentration n_{3D}=1.2x10^{14} cm^{-3}. Small signal Fourier-Transform InfraRed (FTIR) transmission spectroscopy shows inhomogeneously broadened Gaussian 1PA lines with a FWHM of $\Gamma_{FWHM}/2\pi$~ 50GHz. Aluminium contacts of width 0.2cm and separation 0.2 cm were deposited on the sample, which was mounted on a printed circuit board (PCB) and wires were electrically connected using silver paste. A 1V DC bias was applied between the two contacts. The PTIS photo-conductance signal was measured using a current amplifier with gain of 10^3 V/A with a bandwidth of 80MHz.

FELIX produces high intensity, highly tunable radiation in the far infrared (THz) range. The laser light output comes in bursts ("macropulses"), each of which comprises ~100 picopulses with 25MHz repetition rate. The picopulse energy was found from the macropulse energy, monitored continuously with a beam-splitter and a wavelength independent pyroelectric reference detector, calibrated at the end of the experiment with an energy-meter placed just before the last parabolic mirror. The laser light was polarised along a [001] crystal axis. The wavelength of FELIX can be tuned continuously over about one octave without realignment by changing the undulator gap, and further tuning is possible by changing the electron accelerator energy. The centre frequency and bandwidth can monitored continuously using a grating spectrometer with a linear array of pyroelectric detectors, and a small portion of the laser output was picked off for this purpose using a diamond window very close to Brewster's angle (Fig 2). The linear array is rather insensitive and slow, and therefore it was not monitored continuously for every scan – a calibration scan was performed at the start of

the run, producing a small wavelength uncertainty for the individual scans. The FELIX micropulses are very close to transform-limited[44], and the fractional r.m.s. bandwidth Δ_L/ω_L was maintained at about 0.5% (Fig 2) which corresponds to a pulse duration of order 5ps in the 1PA region and 10ps in the 2PA region. The laser produces a small amount of second and third harmonic light with intensities of about 10^{-4} and 10^{-2} of the fundamental respectively, and filters attenuated these by another factor of about 10^{-2} (Fig 2). The filters used were: for 1PA, a 30μm Low Pass Filter; for 2PA, 2.5mm thick quartz; and for 3PA, 3mm sapphire.

Beam intensity

The beam was approximately cylindrically symmetric with Gaussian transverse spatial profile, and so the energy density is $D = D_0 e^{-r^2/r_G^2}$ where D_0 is the density in the centre of the beam and r_G is the radial scale. Half of the energy passes through a radius $r_{1/2} = r_G\sqrt{\ln 2}$, and the full beam energy is $E = \pi r_G^2 D_0$. The beam was focused on the sample between the contacts using a gold-coated, off-axis parabolic mirror. The focussed beam radius, $r_{1/2}$=0.02 cm, was calculated assuming a Gaussian spatial profile. The value of $r_{1/2}$ was confirmed separately by focusing though a pinhole with the sample and cryostat removed.

The excitation due to NPA is non-linear, and although the excitation is strongest in the centre of the beam, the weaker parts of the beam have larger area, so the average NPA excitation occurs in the ring with radius

$$\tilde{r} = \frac{\int_0^\infty r.D^N 2\pi r dr}{\int_0^\infty D^N 2\pi r dr}$$

For a Gaussian beam, $\tilde{r} = 0.5 r_G\sqrt{\pi/N}$ and $\widetilde{D} = D_0 e^{-\tilde{r}^2/r_G^2} = E e^{-\pi/4N}/\pi r_G^2$. The appropriate time-averaged intensity of a Gaussian pulse was given above with Eqn (6),

$$\tilde{I} = \frac{\widetilde{D}}{\tau_G\sqrt{2\pi N^{1/(N-1)}}} = \frac{e^{-\pi/4N}}{\pi^{3/2}\sqrt{2N^{1/(N-1)}}}\frac{E}{r_G^2\tau_G}$$

$\widetilde{D}$ and $\tilde{I}$ are the density and intensity used in discussion of Fig 4.

Care is needed when using an absorption cross-section for an atom in a dielectric medium. We chose to define the cross-section with $\sigma_N = \hbar\omega_{eg} w_N/TI$ where the factor T was included primarily for simplicity, because perturbation theory (Supplementary Materials) produces $w_N = S_N(TI)^N g_N(\Delta)/\hbar\omega_{eg}$ where $T = \mathcal{E}_m^2/\mathcal{E}^2$ is the ratio of the squares of the electric field amplitudes in the medium and vacuum. For atoms in a semi-infinite dielectric with relative permittivity ε_r, with the interface normal to the beam, $T = t_m^2 = 4/[1+\sqrt{\varepsilon_r}]^2$, the square of the Fresnel amplitude coefficient t_m (this is the value of T shown in Table 1). The cross-section might equally be defined $\sigma_N = \hbar\omega_{eg} w_N/I$, or $\sigma_N = \hbar\omega_{eg} w_N/\mathcal{T}I$ where $\mathcal{T} = I_m/I = \sqrt{\varepsilon_r} t_m^2$ is the intensity transmission coefficient, and other definitions are used in situations where the transmission spectrum behind the sample is of interest. Substituting w_N into these alternatives simply leads to a slightly more cumbersome expression on the RHS of Eqn (1), but makes no difference in our effective dipole moment results which rely only on Eqn (6) $P_N = S_N T^N D\tilde{I}^{N-1} g_N(\Delta)/\hbar\omega_{eg}$ which is unambiguous (although it is still important to correctly quantify $T = \mathcal{E}_m^2/\mathcal{E}^2$, see below).

Experimental multi-photon dipole moment analysis

The PTIS photo-conductance signal recorded was a simple average of the current during the macropulse, divided by the DC bias voltage. The spectra in Fig 3 were recorded over a period of a couple of days, during which some changes occurred in the photo-conductance per

photon (due to thermal cycling of the contacts and slight variations in the laser coupling). We divided out the variation in 1PA photo-conductance from the 2PA and 3PA conductance. The measured PTIS photo-conductance signal spectrum, $s_N(\lambda_L)$, was converted to spectral density, $F_N(\lambda_L) = s_N(\lambda_L)/\delta\lambda_L$ where $\delta\lambda_L$ is the point spacing. Each NPA spectrum in Fig 3 shows the spectral density in frequency, which is $F_N(f_L) = cf_L^{-2}s_N(\lambda_L)/\delta\lambda_L$ where c is the speed of light.

In our experiment, the picopulse repetition time is t_{rep} = 40ns, the exponential relaxation time is T_1 ~200ps[45], and the picopulse duration is τ~10ps, i.e. $t_{rep} \gg T_1 \gg \tau$. In this case the excitation averaged over time is $P_N T_1/t_{rep}$ where P_N is the probability of the excited state after the N-photon excitation by a picopulse. Hence the time-average of the photo-conductance signal is $s_N = XT_1P_N/t_{rep}$ where X is a constant related to the density of impurities, the mobility, the bias, the sample geometry and the thermal ionization probability from the excited state. P_N varies across the beam spatial profile due to the variation in the laser energy density D, and this variation must be integrated out to obtain the total N-photon photo-conductance signal, $F_N(\omega) = \int_0^\infty s_N 2\pi r dr$. Integrating over frequency for a single absorption transition to obtain the area under the line shown in Fig 4:

$$Y_N = \int F_N(\omega)d\omega = \frac{XT_1}{t_{rep}} \frac{S_N T^N}{\sqrt{N}\hbar\omega_{eg}\left[\sqrt{2\pi}\tau_G\right]^{N-1}} \int_0^\infty D^N 2\pi r dr$$

where we substituted P_N from Eqn (6) for a Gaussian pulse with $\tilde{I} = D/\tau_G\sqrt{2\pi N^{1/(N-1)}}$ and used $\int_{-\infty}^{\infty} G_N d\omega = 1$.Note that the spectral density in frequency (shown on Fig 3) and angular frequency are related by $F_N(f) = 2\pi F_N(\omega)$, but Y_N is not dependent on the choice of variable for F_N.

For a Gaussian beam spatial profile, $\int_0^\infty D^N 2\pi r dr = E^N / N(\pi r_G^2)^{N-1}$, hence

$$Y_N = \frac{XT_1\sqrt{2}\pi^{3/2}r_G^2}{t_{rep}E_H} \frac{\mu_N}{N^{3/2}} \left(2\frac{E_H}{\hbar\omega_{eg}}\frac{E_H}{\hbar N}\frac{\Delta_L}{\omega_L}\right)^{N-1} \left(\frac{T}{\sqrt{2}\pi^{3/2}}\frac{R_N^2}{a_0^2}\frac{E}{r_G^2}\right)^N$$

where we used $1/\tau_G = 2\Delta_L \approx 2(\omega_{eg}/N)(\Delta_L/\omega_L)$, and we substituted Eqn (4). This last result implies $Y_N \propto E^N$ as shown in Fig 4.

For a pair of 1PA transitions from the 1s ground state to excited states j and k at fixed intensity

$$\frac{Y_1(j)}{Y_1(k)} = \frac{X(j)T_1(j)R_1^2(j)}{X(k)T_1(k)R_1^2(k)}$$

We expect that $X(j) \approx X(k)$ and $T_1(j) \approx T_1(k)$ for excited states j and k if they have similar binding energy. For example $[R_1(2p_\pm)/R_1(2p_0)]^2 = 4$ (Table 2) and $T_1(2p_\pm)/T_1(2p_0) = 0.8$[45] in reasonable agreement with $Y_1(2p_\pm)/Y_1(2p_0)$ from Fig 4, validating the assumption of $X(j) \approx X(k)$.

We can extract values of multi-photon dipole moment R_N from Fig 4 by comparing the NPA transition with a 1PA transition of known R_1 at fixed pulse energy, or we can take advantage of the fact that the multi-photon absorption is so strong it can exceed the 1PA, and the lines intersect. If the integrated photo-currents for the 1PA transition from 1s→k and the NPA transition from 1s→j are both equal, $Y_1(k) = Y_N(j)$, when E=E_X:

$$E_X = \left(N^{\frac{3}{2}-N}\frac{R_1^2(k)/a_0^2}{R_N^{2N}(j)/a_0^{2N}}\right)^{1/(N-1)} \sqrt{\frac{\pi}{2}}\frac{1}{2\alpha_{fs}T}\frac{\omega_L}{\Delta_L}\frac{r_G^2}{a_0^2}\hbar\omega_{jg}$$

We now consider the significant sources of systematic uncertainty the measurement of Fig 4 and the consequent uncertainty in the experimental results in Table 2. First, it is always difficult to make well-calibrated absolute measurements of pulse energy, E, in the THz region of the spectrum. Second, we assumed that the transmission coefficient from vacuum to the sample is simply given by the Fresnel coefficient, T, and we ignored scattering loss and reflection from the back interface, which reduces the effective transmission coefficient. Third, it is difficult to ensure that the spatial profile of a THz beam at the focus of a small f-number off-axis parabolic mirror is Gaussian, as we assumed, which affects $r_{1/2}$. There are some minor contributions to the systematic uncertainty arising from the approximation that the laser beam has Gaussian temporal and spatial beam profiles, and we have assumed that $X(j) \approx X(k)$ for excited states with the same principal quantum number, which ought to be a good approximation when they have similar binding energy. Overall we expect these errors to be much less than an order of magnitude, and it is notable that all the experimental R_N^{2N} values are well within an order of magnitude of the expected scaled atomic unit a_0.

Data Availability Statement (DAS)

The data used in this work are available to download at https://doi.org/10.5281/zenodo.1145706